



# Effect of Ni NP morphology on catalyst performance in non-thermal plasma-assisted dry reforming of methane



Kristy Stanley <sup>a</sup>, Sean Kelly <sup>b</sup>, James A. Sullivan <sup>a,\*</sup>

<sup>a</sup> School of Chemistry, University College Dublin, Belfield Dublin 4, Ireland

<sup>b</sup> School of Biosystems and Food Engineering, University College Dublin, Belfield Dublin 4, Ireland

## ARTICLE INFO

**Keywords:**  
Dry Reforming  
Non-thermal Plasma  
Ni catalysts  
Particle morphology

## ABSTRACT

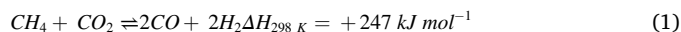
Supported nickel nanoparticle catalysts, with differing nickel morphologies, were studied in the non-thermal plasma-promoted dry reforming of methane. Catalysts with nickel particles containing a greater ratio of (111) lattice planes and surface structures in the nanoscale, *i.e.* dendritic and flake-like particles, showed higher conversions and yields (CH<sub>4</sub> conversions of 65 % and 22 % and CO<sub>2</sub> conversions of 43 % and 33 % respectively with H<sub>2</sub> yields of 42 % and 34 % and CO yields of 31 % and 24 % respectively) than spherical analogues which had conversions of 26 % (CH<sub>4</sub>) and 16 % (CO<sub>2</sub>) and yields of 21 % (H<sub>2</sub>) and 11 % (CO). This is thought to be related to the favourability of (111) faces for CH<sub>4</sub> dissociation and the potential for the formation of micro-discharges around their small surface features. All materials tested showed higher CH<sub>4</sub> conversion and H<sub>2</sub> production when compared with reactions carried out in the absence of a catalyst. The latter reactions showed a greater extent of competing side reactions, resulting in lower conversions and yields.

## 1. Introduction

Shortage of fossil fuels and record levels of greenhouse gas (GHG) are two of the greatest challenges currently facing our society [1]. The combustion of fossil fuels (currently 83 % of global energy demand) is the leading source of CO<sub>2</sub> emissions [2].

The related effects on climate have prompted the Intergovernmental Panel on Climate Change (IPCC) to set global targets to reduce greenhouse gas emissions [3]. The IPCC also state that removal of atmospheric CO<sub>2</sub> *via* carbon capture, storage, and utilisation (CCSU) methods has the potential to remove levels of CO<sub>2</sub> equivalent to those released from anthropogenic sources. Developments in CCSU technology are essential if we are to meet net-zero emission targets.

One such CO<sub>2</sub> utilisation process is the dry reforming of methane reaction (DRM) [4]. The process involves reacting two greenhouse gases; methane and carbon dioxide to form a valuable product, synthesis gas (or syngas).



Syngas is a feedstock for many industrial reactions, including methanol and ammonia synthesis and the Fischer-Tropsch process and a potential fuel.

As an endothermic reaction, the equilibrium process can be used as a thermochemical heat pump. That is, when excess solar or wind generated energy is available, this excess can be used to convert CH<sub>4</sub>/CO<sub>2</sub> mixtures to CO/H<sub>2</sub>. When sources of renewable energies are unavailable, the reverse reaction can be carried out to release energy. Such storage of energy will be a significant requirement to tackle the intermittency inherent in several sources of renewable energy. Such storage will complement storage in batteries.

Losses in efficiency, resulting from conversion of electricity to heat to drive this reaction are a problem.

DRM suffers from many limitations. Temperatures greater than 1000 °C are required for any meaningful conversion, therefore the process is rarely economically viable. At temperatures below 643 °C,  $\Delta G$  is positive and the reaction is non-spontaneous [5]. The reaction is also equilibrium limited.

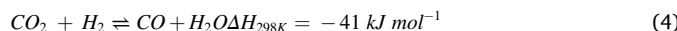
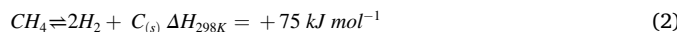
While the need for high temperatures can be somewhat reduced with the use of catalysts, the most active catalysts require critical elements such as Ru, Rh, Ir or Pd [6]. Transition metal catalysts such as those based on Ni, Fe, Mg and Co are also reactive and have been thoroughly researched [7–11], but these have propensities for metal oxidation and sintering and carbon deposition all of which lower reactivity.

Competing side reactions such as methane decomposition (Eq. 2), the

\* Corresponding author.

E-mail address: [james.sullivan@ucd.ie](mailto:james.sullivan@ucd.ie) (J.A. Sullivan).

Boudouard reaction (Eq. 3) and the Reverse Water Gas Shift reaction (Eq. 4) also limit efficiency. These result in unwanted products and catalyst poisoning.



Supported nickel as the active component in a heterogeneous catalyst has been thoroughly researched. To date research has focused on catalysts prepared by the wet impregnation of nickel onto a support material or via atomic layer deposition (ALD). Little work has focused on the deposition of pre-synthesised nickel nanoparticles, or on the effect the NP shapes have on conversion in the DRM reaction. Han et al. [12] and Kim et al. [13] have noted effects relating to Ni particle shape on reactivity.

Research into the use of plasma as a promoting medium for chemical reactions is increasing. Many forms of plasma and reactor configurations including atmospheric, non-thermal (or non-equilibrium) plasma (NTP) have been researched. NTPs are low temperature plasmas generated by passing a high voltage current, through a gas, resulting in ionization of the gas within and the formation of cations, free electrons, and excited species. The large mass difference between the cations and electrons in the gas, mean that little energy is passed from the electrons to the larger species during collisions. This allows the bulk of the gas to remain at room temperature while the 'hot' electrons can have kinetic energies equivalent to 30,000 K.

As a reaction promoter NTP's offer the potential for instantaneous reactivity, removing the time and energy required to reach and maintain high reactor temperatures needed in thermally promoted reactions. Given the fact that an electrical source is needed for plasma generation, this is especially beneficial when considering the use of the reaction considered here as a plasma-promoted thermochemical heat pump to store transiently generated renewable electricity.

The use of plasma to promote the DRM reaction has also been the subject of much research, with many aspects of the reaction parameters and reactor configurations being investigated [14-18]. NTP can be used to promote the reaction in a hybrid system, along with a catalyst. The plasma is generated within the reaction gas mixture, as it flows over the catalyst. This opens up new gas-phase and gas-to-surface-phase reaction pathways [19] through the generation of positively charged ions, electrons, radicals, and excited state species. Liu et al. studied methane conversion over zeolite catalysts with a low temperature plasma and ascribed increased performance to a decreased work function [20,21]. It has also been shown that the plasma can alter the morphology of the catalyst surface, creating surface defects. In semiconductors these defects result in localized changes to the band gap structure which shifts the Fermi level and the free carrier density [22].

The DRM reaction has been studied over a number of wet impregnated Ni catalysts [23-28]. However, its promotion using plasma assisted catalysis over Ni catalysts of different Ni morphology (to discern the effects of Ni morphology) has not. This work aims to fill this gap.

Specifically, we look at nanoparticulate Ni/γ-Al<sub>2</sub>O<sub>3</sub> catalysts, where Ni nanoparticles are first prepared with differing morphologies (spherical, dendrite and flake-like), and then deposited onto a γ-Al<sub>2</sub>O<sub>3</sub> surface. The results highlight the difference in reactivity between these materials in the NTP-promoted dry reforming of methane. To our knowledge investigations into the effect of Ni NP shape on conversion in plasma-promoted DRM has not previously been undertaken.

## 2. Experimental

### 2.1. Synthesis of nickel nanoparticles

The preparation of Ni nanoparticles of varied morphology followed that of Bouremana et al. [29]. Three solutions of NaOH (5 M, 15 M, 25 M) were prepared by dissolving the appropriate mass of NaOH in 20 mL of deionised water. A 0.5 M solution of NiCl<sub>2</sub>·6 H<sub>2</sub>O was prepared by dissolving NiCl<sub>2</sub>·6 H<sub>2</sub>O (1.1885 g) in deionised water (10 mL). 1 mL of this solution and ethylenediamine (EDA) (350 μL, 5.2 mmol) was added to each NaOH solution and stirred vigorously for 60 min. Hydrazine hydrate (125 μL, 8 mmol) was added to each mixture and stirred for a further 30 min. The solutions were then transferred to a 40 mL volume autoclave, and this was placed in a furnace for 4 h at 140 °C. In each case, this treatment resulted in the formation of black particles in a clear solution. The particles were collected using a magnet, washed with deionised water and ethanol, and placed in an oven at 80 °C for 12 h to dry. These preparations resulted in NPs with three differing morphologies; The use of 5 M NaOH gave NPs with a dendrite-like structure (denoted as D-Ni NP), 15 M NaOH gave spherical shaped NPs (denoted as S-Ni NP) and 25 M NaOH gave Ni NPs with a flake-like structure (denoted as F-Ni NP).

### 2.2. Deposition of nickel nanoparticles onto γ-Al<sub>2</sub>O<sub>3</sub>

The synthesised Ni NPs were deposited onto the surface of γ-Al<sub>2</sub>O<sub>3</sub> pellets, at levels sufficient for a nominal loading of 7 wt % Ni, via the manipulation of surface charges as described by Libor et al. [30]. This method is based on the electrostatic attraction of particles with opposite surface charges. These opposite charges are generated by adjusting the pH of suspensions containing Ni NPs and γ-Al<sub>2</sub>O<sub>3</sub>. The γ-Al<sub>2</sub>O<sub>3</sub> pellets (0.152 g) and Ni NPs (0.0106 g) were placed in separate vials containing deionised water (20 mL) and sonicated for 30 min. Concentrated HCl was added dropwise to the γ-Al<sub>2</sub>O<sub>3</sub> suspension until the pH reached 4.3, likewise a solution of NaOH was added dropwise to the Ni NP suspension until pH reached 10.7. The separate suspensions were sonicated for a further 10 min, then mixed and sonicated for 30 min. This resulted in a coating of black particles on the surface of the previously colourless γ-Al<sub>2</sub>O<sub>3</sub> pellets. The coated pellets were vacuum filtered from the suspension, washed with deionised water, and dried in an oven at 80 °C for 12 h. The resulting materials are denoted as D-NiNP/γ-Al<sub>2</sub>O<sub>3</sub>, S-NiNP/γ-Al<sub>2</sub>O<sub>3</sub> and F-NiNP/γ-Al<sub>2</sub>O<sub>3</sub>.

### 2.3. Materials characterisation

X-ray diffraction was used to determine the bulk crystal phase of the Ni NPs and alumina support prior to deposition, and also the Ni/γ-Al<sub>2</sub>O<sub>3</sub> composites, after impregnation. This was performed on a Siemens D500 Kristalloflex Diffractometer with a Cu Kα source ( $\lambda = 0.1541 \text{ nm}$ ), scans were conducted in 20° mode with steps of 0.02°.

The nickel content (wt %) of each material was determined using ICP/MS carried out on an iCAP-Q ICP-MS. Monitored masses were <sup>27</sup>Al and <sup>60</sup>Ni with a dwell time of 20 ms, one peak per mass and 10 sweeps/run for 20 runs.

BET surface area measurements were carried out on a Micrometrics Gemini VII BET analyser, with N<sub>2</sub> as the adsorbate gas at 77.3 K.

Surface morphology and chemical composition of the NPs, support, and Ni/γ-Al<sub>2</sub>O<sub>3</sub> composites were investigated via Scanning Electron Microscopy and Energy Dispersive X-ray, carried out on a Hitachi Regulus 8230 with an accelerating voltage of 1.0 kV under high vacuum.

All materials were analysed using Fourier Transform Infra-red spectroscopy with a Bruker Vertex 70 FTIR spectrometer with a Global IR source and liquid nitrogen cooled Mercury Cadmium Telluride (MCT) detector.

The extent of carbon deposition on the surface of the materials after plasma-promoted reaction testing was examined via thermogravimetric

analysis with online mass spectrometry. These measurements were recorded with a TGA Q500 thermogravimetric balance with an Evolved Gas Analysis (EGA) furnace.

#### 2.4. Catalytic activity testing

The catalytic activity of the materials and support were measured in a non-thermal spark discharge plasma reactor at atmospheric pressure. The in-house built reactor [31] (Fig. 1) was set up with an electrode gap of 12 mm. The plasma was ignited with applied voltages of 9 kV using a pulsing frequency of 100 Hz. Current and voltage could be monitored using a Tektronix P6015A high voltage probe and a Rigol MS07034 oscilloscope. Power inputs varied between 2.1 W and 3.9 W.

The DRM reaction was carried out using twelve pellets of catalytic material and a gas mixture of  $\text{CO}_2$ ,  $\text{CH}_4$  and Ar in a 1:1:3 ratio, flowing at 60 mL/min. Aliquots were analysed *via* GC once a steady state of reactants and products had been reached (as monitored using an online mass spectrometer). A Varian GC-450 gas chromatograph, equipped with a methaniser, and TCD and FID detectors was used for this purpose.

Percentage conversion and yield were calculated using the following equations:

$$\text{CH}_4\text{ Conversion}(\%) = \frac{\text{CH}_4^{\text{in}} - \text{CH}_4^{\text{out}}}{\text{CH}_4^{\text{in}}} \times 100 \quad (5)$$

$$\text{CO}_2\text{ Conversion}(\%) = \frac{\text{CO}_2^{\text{in}} - \text{CO}_2^{\text{out}}}{\text{CO}_2^{\text{in}}} \times 100 \quad (6)$$

$$\text{CO Yield}(\%) = \frac{\text{CO}^{\text{out}}}{\text{CO}_2^{\text{in}} + \text{CH}_4^{\text{in}}} \times 100 \quad (7)$$

$$\text{H}_2\text{ Yield}(\%) = \frac{\text{H}_2^{\text{out}}}{2x\text{CH}_4^{\text{in}}} \times 100 \quad (8)$$

The activity and selectivity of fresh aliquots of each material were tested three times and the average reactivity for each material is presented.

While we do not measure the temperature in the reactor during the plasma-promoted reaction, it is clear that there is no substantial bulk temperature rise during activity. The walls of the reactor are not significantly above room temperature directly following the reaction.

### 3. Results and discussion

#### 3.1. Characterisation

The XRD patterns of the as-synthesised nickel NPs, prior to

deposition on  $\gamma\text{-Al}_2\text{O}_3$ , compared to that of a reference nickel pattern (JCPDS 87-712) can be seen in Fig. 2(a). The three main peaks at 44.7°, 52° and 76.5° relate to the lattice planes (111), (200) and (220) of nickel, with a face centred cubic structure [29]. These patterns are a match to that of the reference nickel pattern. However, the diffractogram of F-Ni NP also shows a peak at 37.6°, related to the presence of  $\text{Ni(OH)}_2$  [32]. We can see from the diffractograms that the 44.7° peak (relating to the (111) plane) is most intense for all materials, however it is relatively higher in the profiles of the dendrite and flake-like particles, indicating there are more (111) lattice planes in those materials than in the spherical samples.

Fig. 2(b) shows the XRD patterns of the  $\gamma\text{-Al}_2\text{O}_3$  support and a reference profile of  $\gamma\text{-Al}_2\text{O}_3$  (JCPDS 29-1486). These profiles match. The largest peaks, located at 37.6°, 45.8° and 66.8° correspond to reflections from the (311), (400) and (440) lattice planes of the  $\gamma$ -alumina spinel structure.

XRD profiles of the composite materials (SI Fig. 1c) show peaks relating to both  $\gamma\text{-Al}_2\text{O}_3$  and the Ni particles. As these materials are in pellet form, of approx. 2 mm diameter, a shift to higher values of  $2\Theta$  in all peaks is seen. This is as a result of the surface of the sample being higher than that of the sample stage. All peaks show a uniform shift of 0.6°.

The BET surface area of all materials is shown in Table 1. These show very similar surface areas for all of the composite materials (253 – 257  $\text{m}^2/\text{g}$ ). Interestingly, the addition of Ni particles to the surface of the support ( $\gamma\text{-Al}_2\text{O}_3$  221  $\text{m}^2/\text{g}$ ) does not lower the measured surface area of the materials. The SA of the materials with deposited Ni is actually higher than that of the support. We believe this effect is relates to the treatment of the material in acid (to generate a surface charge) prior to deposition of Ni. Tran et al. [33] report an increase in pore size and BET surface area of  $\text{Al}_2\text{O}_3$  after treatment in sulfuric acid for 30 mins.

ICP/MS was used to determine the nickel content in each of the catalysts, these results can be seen in Table 2. The intended weight loading of nickel onto the support was 7 wt %. However, these results show that between 2.4 wt % and 2.8 wt % Ni was deposited (and clearly Ni particles also remained in the supernatant).

The SEM images of the nickel NPs, prior to deposition on  $\gamma\text{-Al}_2\text{O}_3$ , at different resolutions, can be seen in Fig. 3(a-e). All images show  $> 5 \mu\text{m}$  agglomerates of smaller particles, possessing features on the nanometre scale and with a wide variety of particle sizes. The morphology of each type of particle is notably different from the others. Those synthesised in 5 M NaOH show a spherical morphology with dendrite-like topography on the particle surface (Fig. 3a, b). Spherical particles with a rough surface topography resulted from using 15 M NaOH during synthesis (Fig. 3c,d) and NPs synthesised in 25 M NaOH appear as amorphous flakes (Fig. 3e,f). It is clear that NaOH concentration during synthesis

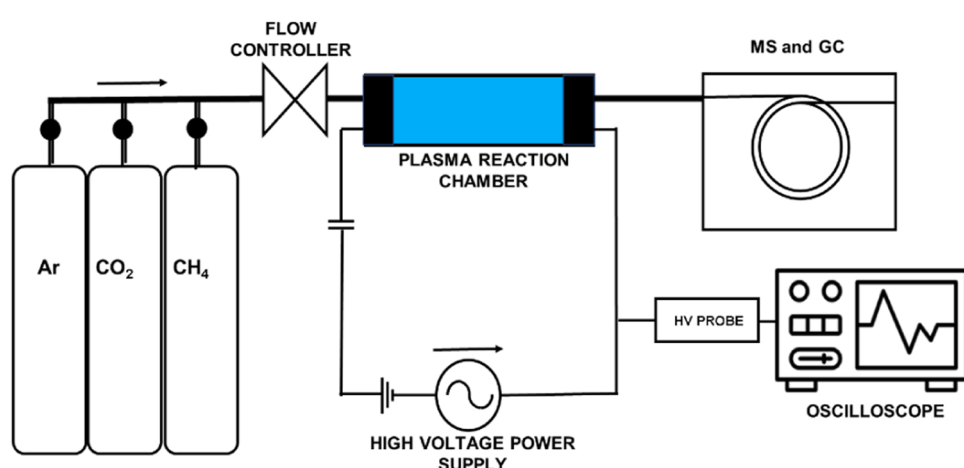
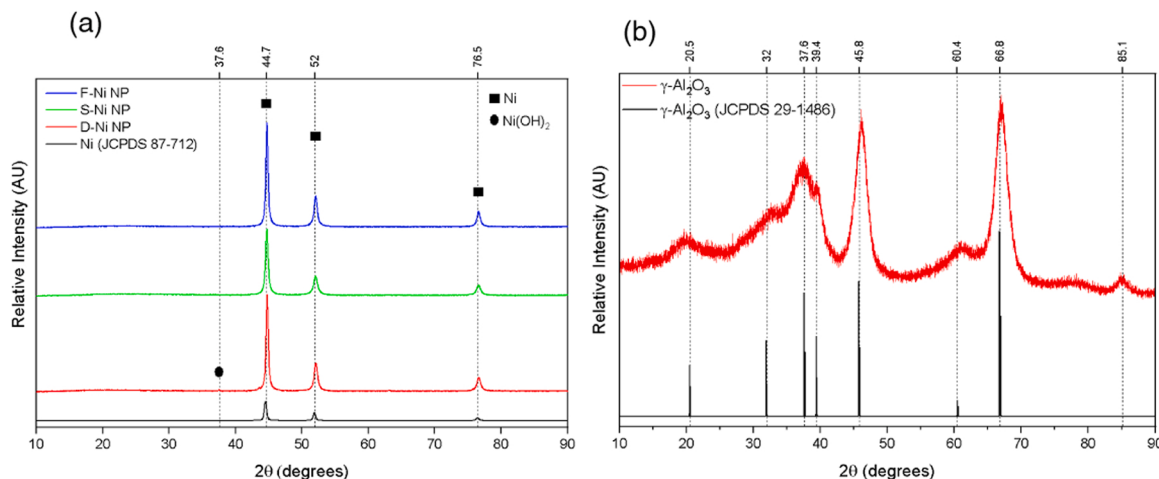


Fig. 1. Schematic of spark-discharge, non-thermal plasma reactor set-up.



**Fig. 2.** a) XRD patterns of Ni NPs prior to deposition on to  $\gamma$ -Al<sub>2</sub>O<sub>3</sub> and nickel reference (JCPDS 87-712), (b) XRD patterns of the  $\gamma$ -Al<sub>2</sub>O<sub>3</sub> support and  $\gamma$ -Al<sub>2</sub>O<sub>3</sub> reference (JCPDS 29-1486).

**Table 1**  
BET surface area measurements of deposited Ni NP composite materials and  $\gamma$ -Al<sub>2</sub>O<sub>3</sub>.

Material	BET Surface Area m <sup>2</sup> /g
D-NiNP/ $\gamma$ -Al <sub>2</sub> O <sub>3</sub>	254
S-NiNP/ $\gamma$ -Al <sub>2</sub> O <sub>3</sub>	257
F-NiNP/ $\gamma$ -Al <sub>2</sub> O <sub>3</sub>	253
$\gamma$ -Al <sub>2</sub> O <sub>3</sub>	221

**Table 2**  
ICP/MS data showing wt % of Ni on each of the Ni loaded materials.

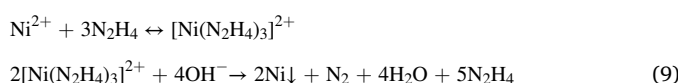
Material	wt % Ni Content
D-NiNP/ $\gamma$ -Al <sub>2</sub> O <sub>3</sub>	2.8 ± 0.056
S-NiNP/ $\gamma$ -Al <sub>2</sub> O <sub>3</sub>	2.4 ± 0.048
F-NiNP/ $\gamma$ -Al <sub>2</sub> O <sub>3</sub>	2.7 ± 0.054

plays a large role in NP growth.

FTIR and difference FTIR was carried out on the Al<sub>2</sub>O<sub>3</sub> support, and the nickel loaded catalysts to confirm modification with Ni after wet-impregnation. These spectra and a related discussion can be seen in the *supplementary information* (SI Fig. 1).

Regarding the different Ni structures formed, the only variable in the preparations was the concentration of NaOH used. As suggested by Ni et al. [34] two nickel complexes are present in solution simultaneously following the reaction between Ni<sup>2+</sup> ions, EDA, and hydrazine, *i.e.* [Ni (en)<sub>3</sub>]<sup>2+</sup> and [Ni(N<sub>2</sub>H<sub>4</sub>)<sub>3</sub>]<sup>2+</sup>. Both complexes are decomposed by OH<sup>-</sup> to form Ni particles. However, the difference in stability and structure between the two complexes means that at lower pH the hydrazine complex reacts first. This results in spherical particles which act as nucleation sites for the next stage of reaction between the EDA complex and OH<sup>-</sup>. As this reaction is slower, the number of nickel atoms available for mass transport to the seed particles is lower, resulting in growth along preferred crystal planes, rather than radially. At higher pH levels, both reactions proceed simultaneously, with the absence of nucleation sites the particle formation yields amorphous shapes.

The reaction between Ni<sup>2+</sup> and hydrazine, to form nickel particles is shown below (Eq. 9), the reaction with EDA proceeds in a similar manner.



This proposal fits well with the results seen here. At lower pH, spheres with dendrite-like surface structures are formed. At higher pH larger, amorphous flake-like particles are formed and at pH values between these, the formed particles are spherical.

EDX analysis (Fig. 4 inset) was also performed on the NPs. The results are all similar and show only the presence of nickel.

### 3.2. Catalytic activity

All materials were tested in the plasma-promoted DRM reaction. A reaction with no catalyst present, was also performed (denoted as plasma-only). The plasma-only experiments were performed at total flow rates of 110 mL/min, rather than 60 mL/min, to equalise the gas residence times within the empty reactor. Each reaction was performed three times (with three plasma on/off cycles as seen in Fig. 4) and the results were averaged to determine conversions and yields.

Fig. 5 shows percentage conversion and yield charts for all materials tested in the plasma-promoted DRM reaction. Conversion and yield values are also shown in Table 3, along with the relevant mole ratios of the products, highlighting the deviation from the expected DRM ratio. The mole ratios were calculated using Eq. 10 below, with the DRM reaction giving an expected value of 1 (as H<sub>2</sub> and CO should be produced in a 1:1 ratio). If the production of hydrogen is greater than CO, this will result in a ratio greater than 1 and indicates that the methane cracking reaction is predominating over CO<sub>2</sub> dissociation. If CO is produced in greater quantities than H<sub>2</sub>, this will result in a ratio lower than 1 and suggests the RWGS reaction is consuming H<sub>2</sub> to produce water. The further this ratio is from 1, the further the reaction is from the pure dry reforming reaction.

$$\frac{H_2}{CO} = \frac{\text{moles } H_2 \text{ produced}}{\text{moles } CO \text{ produced}} \quad (10)$$

CO<sub>2</sub> and CH<sub>4</sub> conversion (and CO and H<sub>2</sub> formation) were noted in all reactions and in all cases more H<sub>2</sub> than CO was produced (suggesting that CH<sub>4</sub> decomposition was a faster process than CO<sub>2</sub> reaction).

The highest reactivity was seen over the D-Ni/ $\gamma$ -Al<sub>2</sub>O<sub>3</sub> material (65 % CH<sub>4</sub>, 43 % CO<sub>2</sub> conversions and 31 % CO, 42 % H<sub>2</sub> yields). This selectivity can be clearly seen in the deviation of product ratio from true DRM (1.35). Reaction over this catalyst showed a H<sub>2</sub>:CO product ratio closer to 1 than all of other reactions.

The flake-like particles were the next most reactive catalyst with the spherical material being the least active of the Ni-containing materials. The deviation from true DRM product ratios following the same trend (1.41 and 1.91).

These differences in activity cannot be attributed to surface area of

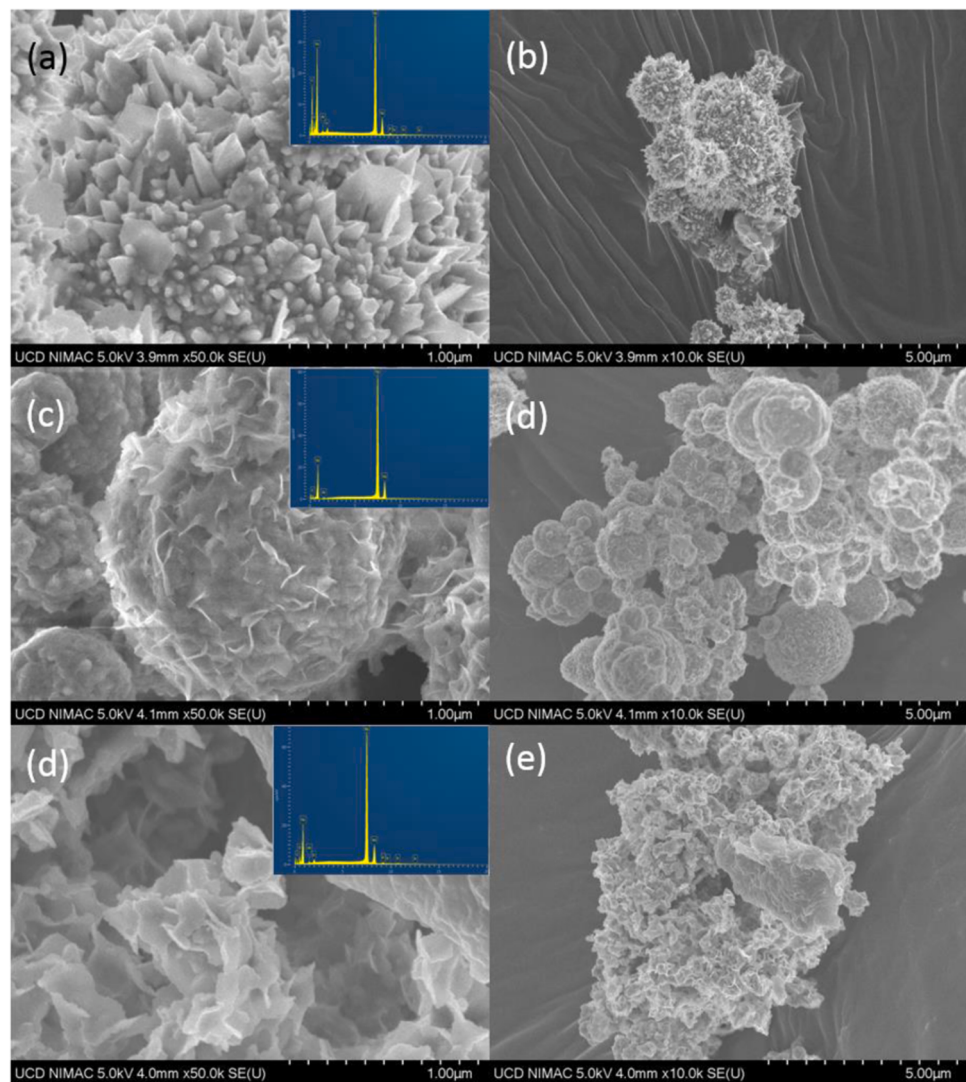


**Fig. 3.** SEM images (inset EDX spectra) of nickel NPs prior to deposition on  $\gamma$ -Al<sub>2</sub>O<sub>3</sub>, with (a, b) dendrite-like, (c, d) spherical and (e, f) flake-like morphologies.

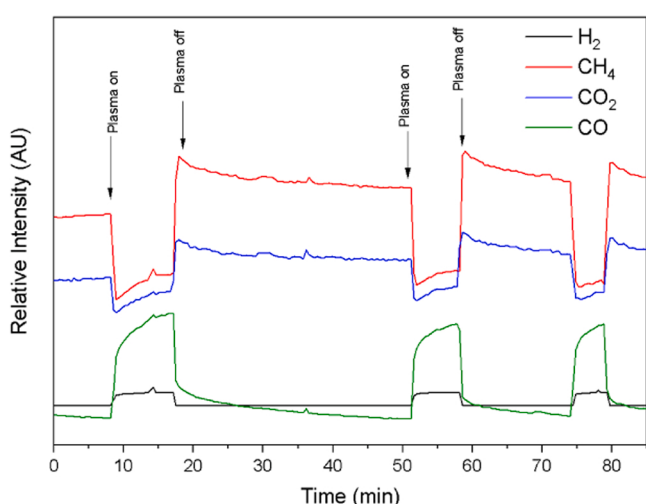


**Fig. 4.** Typical mass spectrometer profiles showing changes in concentrations of interest during plasma on/off cycles in the DRM plasma-only reaction.

the materials, (see Table 1) or due to particle size or nickel loading effects (see Table 2). Therefore, Ni particle morphology must play a large role in the differing activity of the catalysts. XRD suggests the principal difference between these particles is the increased (111) content of the particles dendritic and flake-like particles.

The  $\gamma$ -Al<sub>2</sub>O<sub>3</sub> support showed intermediate reactivity between the more (D and F) and less (S) reactive Ni materials; 34 % CH<sub>4</sub>, 19 % CO<sub>2</sub> conversions, and 15 % CO, 25 % H<sub>2</sub> yields. It also showed deviation from the DRM reaction with more CH<sub>4</sub> conversion (and a product ratio of 1.67).

The plasma-only reactions gave CO<sub>2</sub> and CH<sub>4</sub> conversion at levels of 27 % and 37 % respectively (higher than those seen over Al<sub>2</sub>O<sub>3</sub> and the spherical particles) and CO and H<sub>2</sub> yields of only 8 % and 15 %. This reaction showed the lowest yields of all experiments and a large deviation from the expected DRM product ratios (1.88).

This suggests there is a synergy between the plasma and catalyst (even the lowest performing catalyst) in relation to a mitigating effect against the occurrence of competing side sections (Eqs. 2–4).

The results seen here show greater activity over materials containing nickel particles with more (111) faces. This is consistent with evidence that in the DRM reaction CH<sub>4</sub> dissociation (an integral component of the reaction mechanism) prefers step sites to terraces on the nickel surface [7]. Kim et al. [13] found, in their thermal DRM analysis, that polyhedral NPs (with more (111) surfaces) showed greater activity than

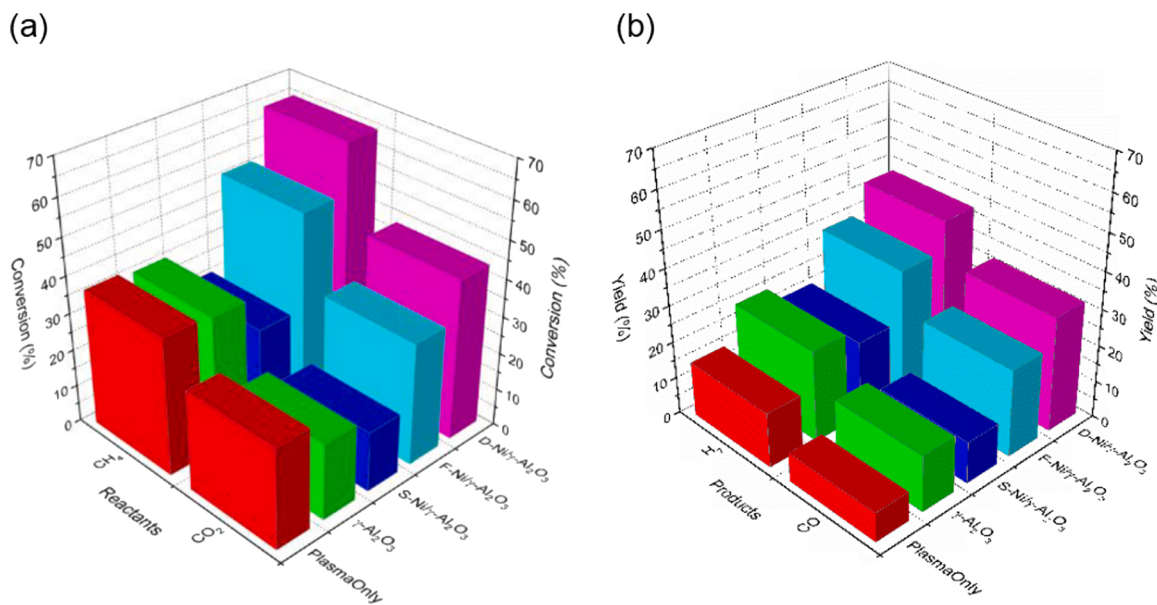


Fig. 5. Bar chart showing (a) percentage conversion of  $\text{CH}_4$  and  $\text{CO}_2$  and (b) percentage yield of  $\text{CO}$  and  $\text{H}_2$  over all materials in the plasma-promoted DRM reaction.

Table 3

Conversion and yield (%) over D-Ni/γ-Al<sub>2</sub>O<sub>3</sub>, F-Ni/γ-Al<sub>2</sub>O<sub>3</sub>, S-Ni/γ-Al<sub>2</sub>O<sub>3</sub>, plasma-only reaction and Ni/γ-Al<sub>2</sub>O<sub>3</sub> catalyst along with product ratio.

Materials	% Conversion		% Yield		H <sub>2</sub> :CO Ratio
	CH <sub>4</sub>	CO <sub>2</sub>	H <sub>2</sub>	CO	
D-NiNP/γ-Al <sub>2</sub> O <sub>3</sub>	65	43	42	31	1.35
F-NiNP/γ-Al <sub>2</sub> O <sub>3</sub>	52	33	34	24	1.41
S-NiNP/γ-Al <sub>2</sub> O <sub>3</sub>	26	16	21	11	1.91
Plasma Only	37	27	15	8	1.88
γ-Al <sub>2</sub> O <sub>3</sub>	36	20	25	15	1.67

hemispherical NPs. This is also consistent with these results where our XRD patterns (Fig. 2a) show that profiles of both the (most active) dendrite and flake-like NPs, have high intensity peaks for reflections from (111) faces.

The S-Ni/γ-Al<sub>2</sub>O<sub>3</sub> material (which has the lowest proportion of (111) faces as measured by XRD) showed the lowest conversion of all reactions tested (26 %  $\text{CH}_4$ , 16 %  $\text{CO}_2$  conversions and 11 %  $\text{CO}$ , 21 %  $\text{H}_2$  yields). This material also showed the greatest deviation from true DRM of all reactions (1.91).

Another potential explanation for the difference in activity between the deposited Ni materials, with regards to their surface morphology, is the possibility of micro-discharges forming around surface structures. As described earlier, Zhang et al. [35] modelled plasma behaviour over a variety of materials and surface structures. They found that for surface pores, below 50  $\mu\text{m}$  in diameter, micro-discharges form, which result in a higher plasma density. This higher density then leads to higher conversions. SEM showed that the dendrite and flake-like materials possess surface structures within this range while the spheres do not. Potentially micro-discharges may be forming around the surface features of these two materials, enhancing plasma density and reactant conversion.

Regarding the extent of  $\text{CH}_4$  and  $\text{CO}_2$  conversion (and the deviation from true DRM), it is clear that in all cases, parallel reactions are taking place alongside the dry reforming reaction. Furthermore, there is no carbon balance between  $\text{CH}_4$  and  $\text{CO}_2$  input, *versus*  $\text{CO}$  and  $\text{H}_2$  yields.

In all cases,  $\text{CH}_4$  conversion and  $\text{H}_2$  production are seen at higher levels than  $\text{CO}_2$  conversion and  $\text{CO}$  formation.  $\text{CH}_4$  decomposition (Eq. 2) (with associated carbon deposition) is occurring as carbon deposits are visible on the surface of the post-reaction catalysts and along the reactor walls following all reactions. The former are quantifiable using

post reaction TGA, but the latter are not. Carbon deposition may also be taking place *via* the Boudouard reaction (Eq. 3).

### 3.3. Post-reaction characterisation

Difference FTIR (D-FTIR) of the post-reaction catalysts was carried out in order to gain insight into any changes to the surface of the material following reaction and these spectra, along with discussion, can be seen in the *supplementary information* (SI Fig. 2). In brief, these show the presence of materials containing C-H, C=C and C=O bonds being added to the surface, while  $\text{H}_2\text{O}$  and surface NiO species are removed from the surface during the reaction.

Post-reaction TGA analysis was carried out on all materials to attempt to assess the extent of carbon deposition during the reaction. Typical results can be seen in Fig. 6 and TGA profiles for all materials, both pre- and post-reaction can be found in the *supplementary information* (SI Fig. 3). Table 4 shows the total percentage weight loss from all materials following TGA and the proportion of this related to deposited carbon combustion. This was estimated by measuring mass loss associated with defined peaks in the DTGA profiles, above 200 °C (where C(s) combustion takes place).

The TGA of all pre-reaction materials all showed an initial weight loss event below 120 °C due to the release of adsorbed water, then a continual decrease in mass across the temperature range due to the condensation of surface hydroxyls (and subsequent formation of bridging oxides and release of  $\text{H}_2\text{O}$ ).

The post-reaction  $\gamma$ -Al<sub>2</sub>O<sub>3</sub> support showed a total weight loss of 9.4 % following TGA. The TGA shows the drop in weight below 100 °C (~ 4 % loss), likely due to surface adsorbed water. The remainder of the mass loss occurs gradually over the temperature range, with no defined peaks in the DTGA showing to a mass loss event, therefore it is not possible to relate this loss directly to carbon combustion. However, the catalyst did show surface discolouration and the peaks in the DFTIR spectrum (SI Fig. 2) of the material showed the appearance of peaks relating to C-H, C=O and C=C bonds.

Of the three supported Ni catalysts the post-reaction F-NiNP/γ-Al<sub>2</sub>O<sub>3</sub> material showed the greatest total weight loss of 12.4 % during TGA. Again, a release below 100 °C, likely of surface water is seen (~ 2.5 % of the total weight). The DTGA shows a small peak between 400 °C and 500 °C which relates to a weight loss of ~1 %. A study carried out by Alipour et al. [36] suggests that this relates to the combustion of amorphous and

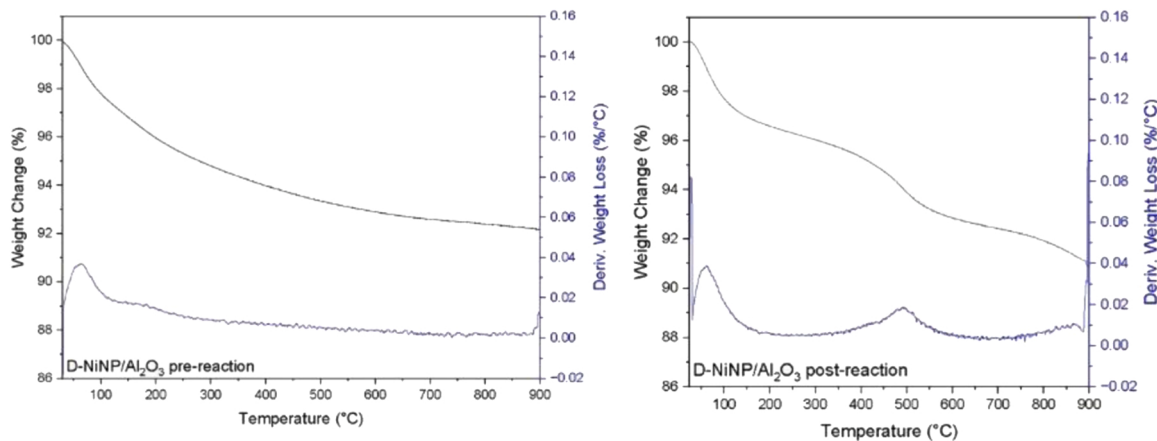


Fig. 6. Pre- and post-reaction TGA/DTGA of D-NiNP/γ-Al<sub>2</sub>O<sub>3</sub>.

Table 4

Pre- and post-reaction weight loss for all materials as measured by TGA and % related to carbon deposition.

Material	Weight Loss (%) Pre-Reaction	Weight Loss (%) Post- Reaction	Weight Loss (%) from Carbon Combustion
D-NiNP/γ-Al <sub>2</sub> O <sub>3</sub>	-7.9	-9.2	1.8
F-NiNP/γ-Al <sub>2</sub> O <sub>3</sub>	-8.8	-12.4	7.5
S-NiNP/γ-Al <sub>2</sub> O <sub>3</sub>	-7.2	-9.8	unconfirmed
γ-Al <sub>2</sub> O <sub>3</sub>	-7.5	-9.4	unconfirmed

graphitic carbon. The TGA/DTGA profile of this material also shows another mass loss above 800 °C of ~5 % of the total weight. Carbon combustion at these temperatures is related to combustion of crystalline forms of carbon [36,37]. The post-reaction FTIR (SI Fig. 2), also shows peaks relating to C–H, C=O, C=C and C=C bonds. Interestingly, although being one of the more active catalysts, this material showed the highest amount of carbon deposition. This may be related to the fact that the XRD pattern for this material shows it to have a high ratio of (111) faces, which are the preferred planes for CH<sub>4</sub> decomposition and the main source of carbon deposition.

The D-NiNP/γ-Al<sub>2</sub>O<sub>3</sub> material, the most active catalyst, gave the lowest overall weight loss (9.2 %) during TGA. Again, an initial rapid weight change of ~4 % below 100 °C is seen, as with the other materials. This is followed by a prominent peak on the DTGA, relating to a weight loss of approx. 1.5 %, between 450 °C and 550 °C (due to combustion of amorphous and graphitic carbon). A small peak on the DTGA, above 890 °C can also be seen and this relates to a mass loss of approx. 0.3 %. We can then say the weight loss due to carbon release in this material is less than 2 %. This is supported by the DFTIR spectrum (SI Fig. 2) of the material which shows little change between the pre- and post-reaction catalysts.

Finally, the least active catalyst, S-NiNP/γ-Al<sub>2</sub>O<sub>3</sub> material, showed a very similar TGA/DTGA profile to that of the γ-Al<sub>2</sub>O<sub>3</sub> material. It had a total weight loss of 9.8 %, with the typical initial weight loss of approx. 4 %, from removal of adsorbed water followed by a gradual weight loss over the remainder of the temperature range. There were no peaks in the DTGA profile. Therefore, none of the weight loss from this material can be directly related to the combustion of surface carbon. On the other hand, the DFTIR spectrum of this material showed evidence of the C–H, C=O and HC=CH bonds on the surface of the material after catalytic testing.

We can see from the TGA results that the extent of carbon deposition

is not related to the activity or selectivity of the catalysts.

#### 4. Conclusion

A range of nickel particles with features in the nanoscale range were synthesised (using various hydrothermal processes), to yield differing nickel particle morphologies. These were deposited onto a γ-Al<sub>2</sub>O<sub>3</sub> support and studied in the plasma-promoted dry reforming reaction.

SEM revealed the particles to have (a) dendrite-like, (b) spherical or (c) flake-like morphologies. Once deposited onto the Al<sub>2</sub>O<sub>3</sub> support, BET and ICP/MS analysis showed the surface area and Ni loadings of the composites to be comparable (253 m<sup>2</sup>/g – 257 m<sup>2</sup>/g, 2.4 – 2.7 wt % Ni).

Regarding reactivity, catalysts with nickel particles containing a greater ratio of (111) lattice planes and surface structures in the nanoscale, *i.e.* dendritic (D) and flake-like (F) particles, showed higher conversions and yields (CH<sub>4</sub> conversions of 65 % and 22 % and CO<sub>2</sub> conversions of 43 % and 33 % respectively with H<sub>2</sub> yields of 42 % and 34 % and CO yields of 31 % and 24 % respectively) than spherical analogues which had conversions of 26 % (CH<sub>4</sub>) and 16 % (CO<sub>2</sub>) and yields of 21 % (H<sub>2</sub>) and 11 % (CO).

This higher activity of the dendrite and flake-like supported materials is thought to be related to the surface structures. XRD confirmed these particles have a greater number of (111) faces which have previously been reported to be favourable for CH<sub>4</sub> dissociation.

Plasma-only reactions showed higher conversions than over spherical Ni particles. CO and H<sub>2</sub> yields were much lower, indicating a greater extent of competing side reactions in the plasma-only case. Thus, the presence of a catalyst in the reactor chamber can direct the reaction selectivity.

Surface structures < 50 μm (as are present in these materials), and it has been reported that these allow the formation of micro-discharges which enhances plasma density. It is also possible that this effect affects reactivity.

Post-reaction FTIR and TGA showed carbon deposition occurred on all materials. The extent of deposition showed no relationship to catalyst activity and there is no relationship between the extent of side reactions and the levels of carbon deposition. The two most active catalysts showed evidence of crystalline carbon deposits.

To our knowledge, this is the first research showing the different effects of the Ni morphology on the plasma-promoted DRM reaction.

#### CRediT authorship contribution statement

JAS conceived of the work, directed the research and was involved in preparation of the manuscript. SK constructed and commissioned the plasma reactor and contributed to initial discussions on the approach. KS prepared and characterised the catalysts, carried out the reactivity

studies, prepared the first draft of the manuscript and contributed to subsequent drafts.

## Declaration of Competing Interest

The authors declare the following financial interests/personal relationships which may be considered as potential competing interests: Kristy Stanley reports financial support was provided by Irish Research Council.

## Data availability

No data was used for the research described in the article.

## Acknowledgements

The authors would like to thank the Irish Research Council (grant code GOIPG/2018/2880) and University College Dublin for funding the project. The authors would also like to thank Mr. D. Molloy for collection of XRD profiles.

## Appendix A. Supporting information

Supplementary data associated with this article can be found in the online version at [doi:10.1016/j.apcatb.2023.122533](https://doi.org/10.1016/j.apcatb.2023.122533).

## References

- [1] R. Monroe, The Keeling Curve. @Keeling\_curve, 2021. <https://keelingcurve.ucsd.edu> (accessed).
- [2] BP. BP Statistical Review of World Energy 2019. 2019. (accessed 2022).
- [3] V.P. Masson-Delmotte, A. Zhai, S.L. Pirani, C. Connors, S. Péan, N. Berger, Y. Caud, L. Chen, M.I. Goldfarb, M. Gomis, et al. IPCC, 2021: Summary for Policymakers. In: Contribution of Working Group I to the Sixth Assessment Report of the Intergovernmental Panel on Climate Change, Cambridge University Press: 2021.
- [4] S.D. Jackson, *Hydrogenation: catalysts and processes*, De Gruyter, 2018.
- [5] S. Arora, R. Prasad, An overview on dry reforming of methane: strategies to reduce carbonaceous deactivation of catalysts, *RSC Adv.* 6 (11) (2016) 18668–18688, <https://doi.org/10.1039/c6ra20450c>.
- [6] P. Ferreira-Aparicio, A. Guerrero-Ruiz, I. Rodríguez-Ramos, Comparative study at low and medium reaction temperatures of syngas production by methane reforming with carbon dioxide over silica and alumina supported catalysts, *Appl. Catal. A, Gen.* 170 (1) (1998) 177–187, [https://doi.org/10.1016/S0926-860X\(98\)00048-9](https://doi.org/10.1016/S0926-860X(98)00048-9).
- [7] B. Abdullah, N.A. Abd Ghani, D.-V.N. Vo, Recent advances in dry reforming of methane over Ni-based catalysts, *J. Clean. Prod.* 162 (2017) 170–185, <https://doi.org/10.1016/j.jclepro.2017.05.176>.
- [8] N.A.K. Aramouni, J.G. Touma, B.A. Tarboush, J. Zeaiter, M.N. Ahmad, Catalyst design for dry reforming of methane: analysis review, *Renew. Sustain. Energy Rev.* 82 (2018) 2570–2585, <https://doi.org/10.1016/j.rser.2017.09.076>.
- [9] S. Kawi, Y. Kathiraser, J. Ni, U. Oemar, Z. Li, E.T. Saw, Progress in synthesis of highly active and stable nickel-based catalysts for carbon dioxide reforming of methane, *ChemSusChem* 8 (21) (2015) 3556–3575, <https://doi.org/10.1002/cssc.201500390>.
- [10] J.-M. Lavoie, Review on dry reforming of methane, a potentially more environmentally-friendly approach to the increasing natural gas exploitation, *Front. Chem.* (2014) 2, <https://doi.org/10.3389/fchem.2014.00081>.
- [11] H.O. Seo, Recent scientific progress on developing supported Ni catalysts for Dry (CO<sub>2</sub>) reforming of methane, *Catalysis* 8 (3) (2018) 110, <https://doi.org/10.3390/catal8030110>.
- [12] J.W. Han, C. Kim, J.S. Park, H. Lee, Highly coke-resistant ni nanoparticle catalysts with minimal sintering in dry reforming of methane, *ChemSusChem* 7 (2) (2014) 451–456, <https://doi.org/10.1002/cssc.201301134>.
- [13] Y.H. Kim, Y. Kang, S. Jo, H. Jeong, D. Neagu, J.-H. Myung, Shape-shifting nanoparticles on a perovskite oxide for highly stable and active heterogeneous catalysis, *Chem. Eng. J.* 441 (2022), 136025, <https://doi.org/10.1016/j.cej.2022.136025>.
- [14] S. Kameshima, K. Tamura, Y. Ishibashi, T. Nozaki, Pulsed dry methane reforming in plasma-enhanced catalytic reaction, *Catal. Today* 256 (1) (2015) 67–75, <https://doi.org/10.1016/j.cattod.2015.05.011>.
- [15] N. Pinhão, A. Moura, J.B. Branco, J. Neves, Influence of gas expansion on process parameters in non-thermal plasma plug-flow reactors: a study applied to dry reforming of methane, *Int. J. Hydrog. Energy* 41 (22) (2016) 9245–9255, <https://doi.org/10.1016/j.ijhydene.2016.04.148>.
- [16] A.H. Khoja, M. Tahir, N.A.S. Amin, Recent developments in non-thermal catalytic DBD plasma reactor for dry reforming of methane, *Energy Convers. Manag.* 183 (2019) 529–560, <https://doi.org/10.1016/j.enconman.2018.12.112>.
- [17] E. Cleiren, S. Heijkers, M. Ramakers, A. Bogaerts, Dry reforming of methane in a gliding arc plasma torch: towards a better understanding of the plasma chemistry, *ChemSusChem* 10 (20) (2017) 4025–4036, <https://doi.org/10.1002/cssc.201701274>.
- [18] M.M. Moshrefi, F. Rashidi, H.R. Bozorgzadeh, M. Ehtemam Haghghi, Dry reforming of methane by DC spark discharge with a rotating electrode, *Plasma Chem. Plasma Process.* 33 (2) (2013) 453–466, <https://doi.org/10.1007/s11090-013-9434-z>.
- [19] K.L. Pan, W.C. Chung, M.B. Chang, Dry reforming of CH<sub>4</sub> with CO<sub>2</sub> to generate syngas by combined plasma catalysis, *IEEE Trans. Plasma Sci.* 42 (12) (2014) 3809–3818, <https://doi.org/10.1109/TPS.2014.2360238>.
- [20] C.-j Liu, R. Mallinson, L. Lobban, Nonoxidative methane conversion to acetylene over zeolite in a low temperature plasma, *J. Catal.* 179 (1) (1998) 326–334, <https://doi.org/10.1006/jcat.1998.2225>.
- [21] E.C. Neyts, A. Bogaerts, Understanding plasma catalysis through modelling and simulation-a review, *Journal of physics D, Appl. Phys.* 47 (22) (2014), 224010, <https://doi.org/10.1088/0022-3727/47/22/224010>.
- [22] G.Y. Kim, J.S. Oh, E.H. Choi, G.S. Cho, S.O. Kang, J. Cho, Work function change on O-plasma treated indium–tin–oxide, *Mater. Sci. Eng.: B* 100 (3) (2003) 275–279, [https://doi.org/10.1016/s0921-5107\(03\)00115-6](https://doi.org/10.1016/s0921-5107(03)00115-6).
- [23] S. Kameshima, K. Tamura, Y. Ishibashi, T. Nozaki, Pulsed dry methane reforming in plasma-enhanced catalytic reaction, *Catal. Today* 256 (2015) 67–75, <https://doi.org/10.1016/j.cattod.2015.05.011>.
- [24] D. Mei, X. Tu, Atmospheric pressure non-thermal plasma activation of CO<sub>2</sub> in a packed-bed dielectric barrier discharge reactor, *Chemphyschem* 18 (22) (2017) 3253–3259, <https://doi.org/10.1002/cphc.201700752>.
- [25] L. Brune, A. Ozkan, E. Genty, T. Visart de Bocarmé, F. Reniers, Dry reforming of methane via plasma-catalysis: influence of the catalyst nature supported on alumina in a packed-bed DBD configuration, *J. Phys. D, Appl. Phys.* 51 (23) (2018), 234002, <https://doi.org/10.1088/1361-6463/aac047>.
- [26] X. Tu, J.C. Whitehead, Plasma-catalytic dry reforming of methane in an atmospheric dielectric barrier discharge: Understanding the synergistic effect at low temperature, *Appl. Catal. B, Environ.* 125 (2012) 439–448, <https://doi.org/10.1016/j.apcatb.2012.06.006>.
- [27] D. Lasić Jurković, J.-L. Liu, A. Pohar, B. Likozar, Methane dry reforming over Ni/Al<sub>2</sub>O<sub>3</sub> catalyst in spark plasma reactor: linking computational fluid dynamics (CFD) with reaction kinetic modelling, *Catal. Today* 362 (2021) 11–21, <https://doi.org/10.1016/j.cattod.2020.05.028>.
- [28] Y. Diao, X. Zhang, Y. Liu, B. Chen, G. Wu, C. Shi, Plasma-assisted dry reforming of methane over Mo<sub>2</sub>C–Ni/Al<sub>2</sub>O<sub>3</sub> catalysts: effects of β-Mo<sub>2</sub>C promoter, *Appl. Catal. B, Environ.* 301 (2022), 120779, <https://doi.org/10.1016/j.apcatb.2021.120779>.
- [29] A. Bouremana, A. Guittoum, M. Hemmous, D. Martínez-Blanco, P. Gorria, J. A. Blanco, N. Benrekaa, Microstructure, morphology and magnetic properties of Ni nanoparticles synthesized by hydrothermal method, *Mater. Chem. Phys.* 160 (2015) 435–439, <https://doi.org/10.1016/j.matchemphys.2015.05.015>.
- [30] Z. Libor, Q. Zhang, The synthesis of nickel nanoparticles with controlled morphology and SiO<sub>2</sub>/Ni core-shell structures, *Mater. Chem. Phys.* 114 (2–3) (2009) 902–907, <https://doi.org/10.1016/j.matchemphys.2008.10.068>.
- [31] S. Kelly, J.A. Sullivan, CO<sub>2</sub> decomposition in CO<sub>2</sub> and CO<sub>2</sub>/H<sub>2</sub> spark-like plasma discharges at atmospheric pressure, *ChemSusChem* 12 (16) (2019) 3785–3791, <https://doi.org/10.1002/cssc.201901744>.
- [32] A. Bouremana, A. Guittoum, M. Hemmous, B. Rahal, J.J. Sunol, D. Martínez-Blanco, J.A. Blanco, P. Gorria, N. Benrekaa, Crystal structure, microstructure and magnetic properties of Ni nanoparticles elaborated by hydrothermal route, *J. Magn. Magn. Mater.* 358–359 (2014) 11–15, <https://doi.org/10.1016/j.jmmm.2014.01.036>.
- [33] T.P. Tran, Y. Guo, J. Chen, L. Zhou, M. Sakurai, H. Kameyama, Effect of pore widening treatment on BET surface area of rapidly anodized alumina support, *J. Chem. Eng. Jpn.* 41 (11) (2008) 1042–1048, <https://doi.org/10.1252/jcej.08we025>.
- [34] X. Ni, Q. Zhao, H. Zheng, B. Li, J. Song, D. Zhang, X. Zhang, A Novel Chemical Reduction Route Towards the Synthesis of Crystalline Nickel Nanoflowers from a Mixed Source, Vol. 2005, WILEY-VCH Verlag, Weinheim, 2005, pp. 4788–4793.
- [35] Y.-R. Zhang, E.C. Neyts, A. Bogaerts, Influence of the material dielectric constant on plasma generation inside catalyst pores, *J. Phys. Chem. C* 120 (45) (2016) 25923–25934, <https://doi.org/10.1021/acs.jpcc.6b09038>.
- [36] Z. Alipour, M. Rezaei, F. Meshkani, Effect of alkaline earth promoters (MgO, CaO, and BaO) on the activity and coke formation of Ni catalysts supported on nanocrystalline Al<sub>2</sub>O<sub>3</sub> in dry reforming of methane, *J. Ind. Eng. Chem.* 20 (5) (2014) 2858–2863, <https://doi.org/10.1016/j.jiec.2013.11.018>.
- [37] A.H. Fakheeha, W.U. Khan, A.S. Al-Fatesh, A.E. Abasaeed, Stabilities of zeolite-supported Ni catalysts for dry reforming of methane, *Chin. J. Catal.* 34 (4) (2013) 764–768, [https://doi.org/10.1016/S1872-2067\(12\)60554-3](https://doi.org/10.1016/S1872-2067(12)60554-3).